Zhou *et al. Microstructures* 2023;3:2023043
DOI: 10.20517/microstructures.2023.38

Microstructures

Review

Open Access

Check for updates

Cryogenic atom probe tomography and its applications: a review

Ziyang Zhou[1,2,4], Zhengquan Wang[2,3,4], Ranming Niu[2,5], Pang-Yu Liu[2,5], Chao Huang[2,5], Yi-Hsuan Sun[2,6], Xiutong Wang[4], Hung-Wei Yen[6], Julie M. Cairney[2,5], Yi-Sheng Chen[4,5,6]

[1]State Key Laboratory for Strength and Vibration of Mechanical Structures, School of Aerospace Engineering, Xi'an Jiaotong University, Xi'an 710049, Shaanxi, China.
[2]Australian Centre for Microscopy and Microanalysis, The University of Sydney, Sydney 2006, Australia.
[3]Shaanxi Key Laboratory of Biomedical Metallic Materials, Northwest Institute for Non-Ferrous Metal Research, Xi'an 710016, Shaanxi, China.
[4]Key Laboratory of Marine Environmental Corrosion and Bio-Fouling, Institute of Oceanology, Chinese Academy of Science, Qingdao 266071, Shandong, China.
[5]School of Aerospace, Mechanical and Mechatronic Engineering, The University of Sydney, Sydney 2006, Australia.
[6]Department of Materials Science and Engineering, National Taiwan University, Taipei 106216, Taiwan.

Correspondence to: Prof. Yi-Sheng Chen, Australian Centre for Microscopy and Microanalysis, The University of Sydney, Sydney 2006, Australia. E-mail: yi-sheng.chen@sydney.edu.au

How to cite this article: Zhou Z, Wang Z, Niu R, Liu PY, Huang C, Sun YH, Wang X, Yen HW, Cairney JM, Chen YS. Cryogenic atom probe tomography and its applications: a review. *Microstructures* 2023;3:2023043. https://dx.doi.org/10.20517/microstructures.2023.38

Received: 1 Aug 2023 **First Decision:** 13 Sep 2023 **Revised:** 18 Sep 2023 **Accepted:** 27 Sep 2023 **Published:** 13 Nov 2023

Academic Editors: Lin Gu, Jiangyu Li **Copy Editor:** Fangling Lan **Production Editor:** Fangling Lan

Abstract

Cryogenic atom probe tomography (cryo-APT) is a new microstructure characterization technique with the potential to address challenges across various research fields. In this review, we provide an overview of the development of cryo-APT and the associated instrumentation that transforms conventional APT into cryo-APT. We start by introducing the APT principle and the instrumentation involved in the cryo-APT workflow, emphasizing the key techniques that enable cryo-APT specimen preparation. Furthermore, we shed light on the research made possible by cryo-APT, presenting several recent outcomes to demonstrate its capabilities effectively. Finally, we discuss the limitations of cryo-APT and summarize the potential research areas that can further benefit from this cutting-edge microstructural characterization technique.

Keywords: Atom probe tomography, cryogenic microscopy, microanalysis, materials characterization, hydrogen mapping

© The Author(s) 2023. **Open Access** This article is licensed under a Creative Commons Attribution 4.0 International License (https://creativecommons.org/licenses/by/4.0/), which permits unrestricted use, sharing, adaptation, distribution and reproduction in any medium or format, for any purpose, even commercially, as long as you give appropriate credit to the original author(s) and the source, provide a link to the Creative Commons license, and indicate if changes were made.

INTRODUCTION

Atom probe tomography (APT) is an advanced microanalysis technique that offers a remarkable way to visualize the distribution of atoms within materials at the nanoscale in three dimensions (3-D)[1-4]. It boasts an impressive sub-nanometer spatial resolution and a high chemical resolution. The latter enables it to achieve precision levels of approximately 20 atomic parts per million (at. ppm) for all elements, regardless of their atomic masses[2,5]. The combination of these unique abilities allows the research on the distributions of elements in materials, including those with low atomic mass, such as hydrogen, carbon, and lithium, which are difficult to analyze using conventional optical or electron microscopes[6-8].

In 1955, Müller made a significant breakthrough by developing and utilizing a field ion microscope (FIM), which laid the groundwork for the APT technique[9]. Using the FIM, they observed tungsten atoms on a tungsten tip surface and achieved the world's first atomic-scale image with an unprecedented magnification of over 10^6 times[10]. Later, in 1968, Müller *et al.* further developed the atom-probe FIM[1], integrating a mass spectrometer, which enabled the measurement of the time-of-flight (ToF) of evaporated ions and their mass-to-charge ratios (m/z). This addition provided a chemical resolution to complement the high spatial resolution of the FIM[11]. In 1970, Brenner and McKinney[12] also made a significant contribution to the development and application of FIM and APT for the advancements in surface science.

Over the following decades, the continuous improvement in computational power facilitated computer-assisted experimentation, leading to the development of modern APT instruments. The automation of ion evaporation experiments, data acquisition, and tomographic reconstruction became possible. The first commercial APT instrument was developed by the research group at the University of Oxford in the early 1990s[13], which later led to the foundation of Oxford Nanoscience Ltd. with their products of Position-Sensitive Atom Probe and the subsequent Energy-Compensated Position-Sensitive Atom Probe. In 2001, Imago Scientific Instruments introduced the commercial APT module, making the APT technique more accessible to researchers[14]. In 2006, Oxford Nanoscience was acquired by Imago Scientific Instruments. Subsequently, AMETEK acquired Imago Scientific Instruments in 2010 and merged it with CAMECA, which became the sole APT instrument manufacturer to date. Since Müller's pioneering work in the 1950s, APT has found extensive use in various fields of research and development. Figure 1 depicts the increasing number of APT-related publications by year in the Web of Science database, reflecting the growing adoption of APT analyses. This technique has made significant contributions to advancements in materials science[7,15], biology[16], chemistry[17], physics[18,19], geoscience[20], medicine[21], and energy science[15].

As depicted in Figure 2, to induce this field evaporation, a needle-shaped specimen with a tip diameter less than 100 nm is necessary. The required sharp tips can be created using either electropolishing or focused ion beam (FIB) annular milling techniques[22]. In the APT process, a high voltage of 2-15 kilovolts (kV) is applied to the needle specimen, generating a powerful electric field at the apex of the tip. This electric field is strong enough to strip the outer-shell electron(s) from the atoms at the apex and ionize them. Once ionized, the charged particles are directed by the electric field toward a grounded, time-sensitive detector. The time taken for the ions to travel from the evaporation point to the detector gives the ToF information. To precisely determine the timing of the evaporation process, controlled pulsing with a marginal energy input is applied to the APT tip specimen. The tip is at a constant high voltage of several thousand volts, which is close to the threshold of the level required for field evaporation, and the ion evaporation only takes place when the additional pulsing energy is applied. This energy pulsing can be achieved by using either of the two methods -voltage pulsing and laser pulsing using a focused beam shed on the apex of the specimen, which leads to voltage mode and the laser mode of modern APT, respectively[23].

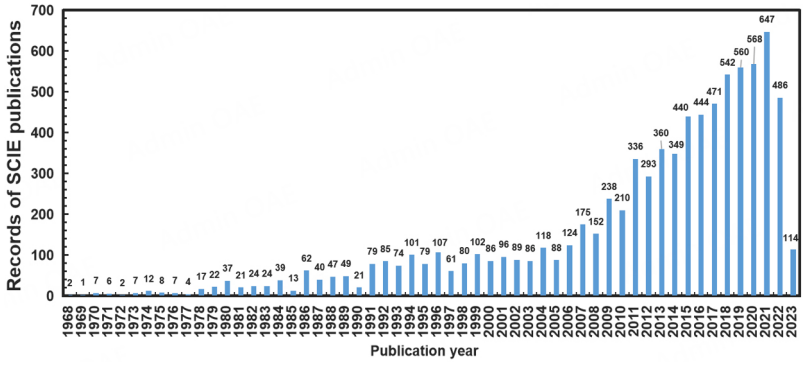

Figure 1. Numbers of Web of Science publications by year using a search term of "atom probe".

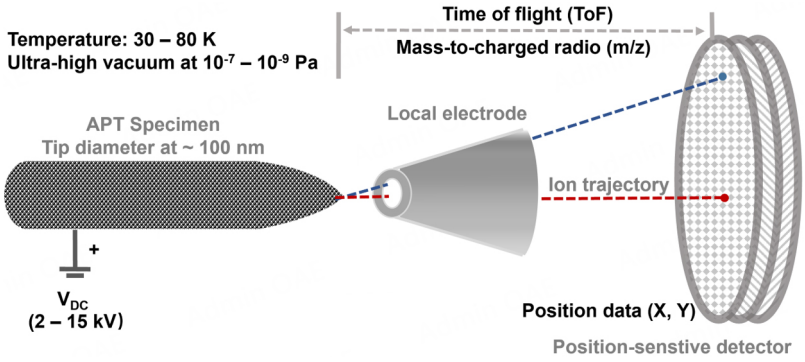

Figure 2. Schematic illustration of the principle and essential components of APT.

Both modes of APT experiments require conducting the analysis on a cryogenic stage [Figure 2] at a temperature range of 30 to 80 Kelvin (K). This low temperature is crucial to minimize thermal vibrations that could otherwise compromise the spatial resolution of the final ion images. In the case of laser-pulsing APT, special attention is needed because the laser beam can potentially heat up the apex, causing the actual tip temperature to deviate from the set temperature. To deduce the m/z of the detected ions in APT, the ToF and the flight path (L) of the APT instrument are taken into account. The m/z values are derived from the conservation of electric potential energy (E_e) and kinetic energy (E_k) of the ions, represented by the equation:

$$E_e = QeV = E_k = \frac{1}{2} mv^2$$

where Q represents the ionization state of the ion, e is the fundamental electric charge, V is the voltage at which ion evaporation takes place at the tip, m is the mass of the ion, and v is the speed of the ion from the tip to the detector over the flight length (L) during a ToF measurement. The m/z can be related to ToF (t) through:

$$\frac{m}{z} = 2eV \left(\frac{t}{L}\right)^2$$

Apart from providing excellent chemical resolution, the APT analysis also offers valuable spatial information. This is achieved by using a position-sensitive ion detector that enables the back projection of the spatial origins of ions based on the nominal ion trajectory path in the equipment [Figure 2][1,2]. As a result, a 3-D reconstructed atom map is produced, providing a detailed visualization of the atomic arrangement within the material under investigation.

To achieve the ultra-high vacuum required for ion evaporation and detection, the modern Local Electrode Atom Probe instrument (LEAP, developed by CAMECA) employs a three-chamber system[13]. The first chamber, known as the “load lock”, is responsible for pumping down from ambient pressure to around 10^{-5} Pa. Once this step is completed, the APT specimen can be transferred to the second chamber, called the “buffer” chamber, which maintains a constant pressure of approximately 10^{-7} Pa. Finally, the APT specimen is moved to the "analysis chamber", where the pressure is maintained below 10^{-9} Pa. This chamber is equipped with various components, including the specimen cooling system, the ion detector for ToF measurements, and the pulsing system.

In 2017, the groundbreaking development of cryogenic electron microscopy (cryo-EM) was honored with the Nobel Prize in Chemistry[24]. This prestigious award recognized the seminal progress made in cryogenic specimen handling, enabling electron microscopy specimens to be rapidly cooled to extremely low temperatures and maintained in a "frozen" state throughout the transfer process. The key to this advancement lies in the ability to quickly quench the specimens, leading to the formation of amorphous ice from the water within them. This amorphous ice prevents ice crystallization, which could otherwise damage delicate structures during slow cooling processes[25]. The innovation in cryo-specimen transfer has opened up exciting possibilities for preserving biological specimens in their natural states before observation in electron microscopes[26]. This breakthrough also served as inspiration for the development of a cryo-specimen handling workflow dedicated to APT by Gerstl and Wepf[27]. This adaptation of cryogenic techniques created opportunities to apply APT to soft matter and specimens containing diffusive solutes, which require low temperatures to immobilize them. Following their pioneering work at ETH Zurich, other APT laboratories have invested substantial efforts in enhancing and innovating cryo-workflows and applications, leading to the emergence of a new microanalysis technique called cryogenic APT (cryo-APT)[28-32]. This cutting-edge approach represents a promising frontier in the field of microanalysis.

CRYO-APT

When it comes to cryo-APT analysis, the critical aspect lies in maintaining the low temperature of the specimen between its preparation and the actual APT analysis. This involves two key processes: the "cryo-transfer" (cryogenic transfer) to keep the specimen at a low temperature and the "cryo-specimen fabrication" to create the specific APT tip geometry. It is important to mention that the temperatures used for cryo-specimen fabrication and cryo-transfer can vary depending on the purpose, the type of coolant used, and the efficiency of thermal conduction from the coolant. Generally, temperatures ranging from 120 to 140 K are required for forming vitrified ice, which helps prevent damage during ice crystallization in biological specimens[26]. On the other hand, temperatures around 150 K are necessary to inhibit the desorption of diffusive hydrogen solute from a metallic specimen[33,34].

The cryo-transfer process involves plunge-freezing or direct cooling in liquid nitrogen, which allows the specimen to reach temperatures as low as 77 K. Using liquid helium enables reaching even lower temperatures of around 4 K. However, in an indirect cooling process, the lowest temperature that the specimen can achieve is somewhat compromised due to limitations in thermal conduction efficiency at various interfaces of the physical components. As a rule of thumb, utilizing copper bands for cooling with

liquid nitrogen can reach temperatures as low as 120 K. These experimental details are crucial to enable successful cryo-APT analysis and open up new possibilities for research in this field.

Cryo-transfer

The success of cryo-transfer for cryo-APT tips depends on three critical factors: environmental moisture that may come into contact with cryo-specimens, the cooling process, including potential heat absorption from the surroundings to the cryo-specimens, and the evacuation process required to reach the UHV levels necessary for the APT experiment[29,35]. Out of these factors, the presence of moisture in the working space is particularly crucial in cryo-APT experiments. When a sharp tip is exposed to moisture, it can lead to frost formation on the surface of the tip, which compromises the required sharpness for APT field evaporation[36]. Therefore, it is imperative to conduct cryo-transfer for APT specimens in an extremely dry environment. This can be achieved by using a glovebox purged with dry, non-reactive gases such as nitrogen and argon. Figure 3A provides an example image of a glovebox used for cryo-APT.

After preparing and treating the specimen inside a glovebox, the next step in cryo-APT involves transferring the cooled specimen from the glovebox to either a FIB system for further tip-shaping or directly to the APT measurement setup. To accomplish this, a specimen loading mechanism is utilized. As shown in the inset of Figure 3A, this connection is achieved using a vacuum specimen carrier, often referred to as a "suitcase". The suitcase is equipped with a specimen stage containing a cold finger that connects to a dewar (indicated by the blue arrow). The cryo-and-vacuum suitcase requires a docking mechanism to connect it to the glovebox (shown as red circles in Figure 3A). Before the cryo-specimen is transferred into the suitcase through a loadlock (indicated by the green arrow in Figure 3A). The loadlock needs to be pre-evacuated to sufficiently low pressure, similar to that of the loadlock of the APT instrument, typically between 10^{-5} and 10^{-6} Pa. This ensures a seamless transition of the specimen into the APT vacuum chambers. Additionally, the loadlock of the glovebox must be connected to a dewar (blue arrow in Figure 3A) that can be filled with coolant to cool the specimen docking stage before it comes into contact with the cryo-specimen[34]. Once the specimen reaches the desired low temperature and pressure, it is removed from the loadlock using a long magnetic-coupling transfer arm (the long rod on the left side of the inset in Figure 3A).

During the process of removing the specimen, the transfer arm operating at room temperature can inadvertently introduce heat, jeopardizing the cryogenic state of the specimen. To counteract this issue, it is necessary to use a thermos-insulating washer, which can be made of polyetheretherketone (PEEK), as shown by the red arrow in Figure 3B, which also shows the APT specimen carrier "puck" (the orange component) for commercial LEAP instruments. In commercial LEAP systems, a carousel is employed to facilitate the movement of specimens across various chambers, including the loadlock, buffer, and analysis chambers. To handle cryo-specimens, the carousel also requires a thermo-insulating adaptation. Figure 3C illustrates the need for a special carousel with a cryo-specimen docking slot made of PEEK to ensure proper cryo-transfer (red arrow). In addition to the cryo-transfer workflow shown in Figure 3 at the University of Sydney, Perea *et al.* developed a vacuum-cryo-transfer system at the Pacific Northwest National Laboratory in the US, which allows APT tips to expose a range of reactive gases such as hydrogen, oxygen, and carbon monoxide[28]. This new instrumentation opens up the possibility of applying APT for catalytic research at the nanoscale, relatable to the dimension of APT tips.

Using the specialized cryo-transfer components mentioned earlier, a typical workflow for pre-sharpened tip specimens mounted on a puck unfolds as follows: Firstly, the specimen undergoes the desired treatment process inside the glovebox, such as electrolytic hydrogen charging as demonstrated in[33,34]. Subsequently, the specimen is directly plunge-frozen in liquid nitrogen and then loaded into the pre-cooled loadlock of

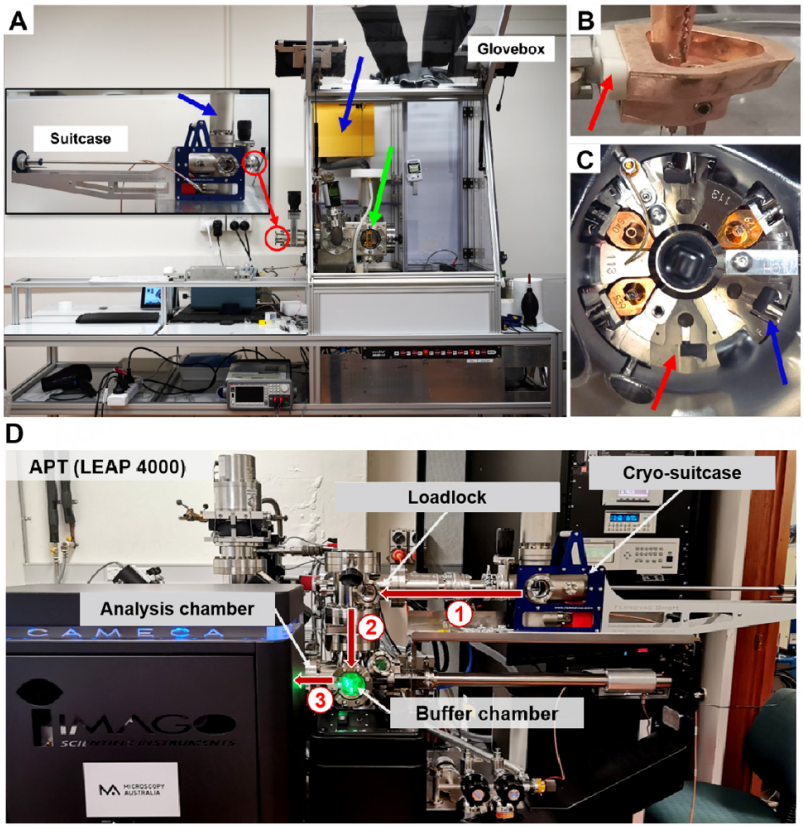

Figure 3. Auxiliaries for enabling cryogenic APT specimen transfer. (A) Glovebox with a dewar (blue arrow) and a loadlock (green arrow) with a cooling stage and turbo pump. The inset shows a specimen-transfer suitcase (by Ferrovac) equipped with a cooling finger connecting to a dewar (blue arrow). Red circles show the docking port connecting the loadlock and the suitcase. (B) Cryo-puck with a thermo-insulating washer (red arrow). (C) Cryo-carousel compatible with commercial APT system (LEAP by CAMECA) with a slot dedicated to cryo-specimen (red arrow), which is distinct from a normal metallic slot (blue arrow). (D) Commercial APT instrument (LEAP 4000 XS) with a suitcase attached.

the glovebox (indicated by the green arrow in Figure 3A). The loadlock is indirectly cooled with a cold finger, which needs to be pre-evacuated to sufficiently low pressure typically between 10^{-5} and 10^{-6} Pa, which is similar to the level of the loadlock of a commercial APT instrument. The puck, containing the cryo-specimens, is then evacuated within the loadlock before being transferred to the pre-cooled vacuum suitcase [Figure 3A inset] using the transfer arm. Next, the entire suitcase, along with the cryo-specimen, is transported to the APT instrument. A docking port is essential for accepting the specimen transferred from the suitcase (Arrow #1 in Figure 3D). Once the suitcase is connected to the APT loadlock, the cryo-specimen is moved into the pre-cooled PEEK slot within the cryo-carousel [Figure 3C]. The cryo-carousel is then shifted into the buffer chamber (Arrow #2 in Figure 3D) before loading the cryo-puck/specimen into the cryo-stage in the analysis chamber for APT measurement (Arrow #3 in Figure 3D). To measure the specimen temperature, a method utilizing the temperature response of the cryo-stage after cryo-specimen loading was demonstrated in[34].

Cryo-specimen fabrication

The process of cryo-APT specimen fabrication is complex due to its stringent geometric requirements. The specimen must have a tip diameter of less than 100 nanometers while maintaining a low-temperature working condition. Electropolished metallic specimens with good mechanical strengths (see[37,38] for electropolishing) can undergo direct plunge-freezing in coolants after treatments such as deuteration[33,34]

and corrosion[39]. After treatment, these specimens can proceed with cryo-transfer[33,34,40]. However, this pre-sharpening method is most effective when the materials being studied have uniform distribution and high density of microstructural features of interest, such as nanosized precipitates or grain boundaries (GBs) in fine-grain materials[33,34,40]. For specimens that require extracting a specific region of interest (ROI) from a bulk specimen, it is essential to use a FIB fabrication method that is compatible with low temperatures, often referred to as cryo-FIB[41-46].

Cryo-FIB necessitates cooling not just the specimen stage but also the lift-out micromanipulator[39]. Both can be achieved by connecting a flexible copper cold band finger to the coolant[36]. The process of FIB lift-out involves trenching and extracting the ROI in a bar [Figure 4A1]. Subsequently, the bar is attached to the micromanipulator, which requires using a gas injection system (GIS) and targeted electron beam deposition to create the attachment or weld. Typically, this weld is made of platinum or carbon. After attachment to the micromanipulator, the bar is removed from the trench and placed onto the pre-sharpened microposts for further tip shaping.

However, working with both the specimen and the micromanipulator at cryogenic temperatures presents a challenge. The GIS deposition cannot function as usual since the injected gas will non-selectively condense onto the surfaces of both the specimen and the micromanipulator, hindering the site-specific attachment[22]. To address this challenge, Schreiber *et al.* developed a method to lift out and attach a frozen specimen onto the micromanipulator and the cooled micropost[39]. They utilized debris from the ion milling process of the cryo-specimen, which can re-deposit/condense onto the low-temperature surfaces. This creates site-specific nano-welds, enabling the cryo-specimen attachment to the micromanipulator and pre-sharpened micropost without requiring the GIS [Figure 4A2-A5]. This innovative method was successfully used to attach a lift-out bar containing frozen water and water-corroded glass onto a silicon (Si) micropost [Figure 4A6]. This breakthrough allowed for the fabrication and analysis of an APT tip incorporating both frozen water and corroded glass [Figure 4B1 and B2] after annular milling.

For cryo-specimens where the ROIs are not buried and are identifiable at the surface of the specimen (as shown in Figure 4), El-Zoka *et al.* developed a method using plasma FIB (PFIB)[32,47]. PFIB offers higher ion milling efficiency compared to conventional gallium FIB, allowing for direct shaping of a tip from the surface of a bulk specimen. This approach avoids the need for a cryo-manipulator and cryo-attachments. The bulk specimen they worked with was nanoporous gold (NPG), which is inherently conductive and, hence, suitable for the APT field evaporation experiment. Additionally, the NPG incorporated frozen heavy water (D_2O ice) as the specimen for analysis within its nanopores[32] (see[15] for the need of using heavy water). The scanning electron microscope (SEM) images displayed in Figure 5 illustrate the specimen preparation process, showing the NPG before tip shaping [Figure 5A], during sharpening [Figure 5B], and after tip fabrication at low and high magnifications [Figure 5C and D, respectively]. The use of PFIB in cryo-preparation has expanded the possibilities for APT analysis of nanosized specimens that can be carried in water and subsequently frozen in ice[32,47].

Besides the mentioned developments in cryo-FIB specimen preparation, significant progress has also been achieved in the cryo-electron microscopy community[48-52]. On the APT side, there are noteworthy outcomes that deserve attention, such as those for biomineral materials[53-58], poly(3-alkylthiophene)[58,59], biomolecules adhered on aluminum substrate tips[60], ferritin embedded in epoxy resin[61], immunoglobulin (IgG) embedded in a silica glass matrix[62], and mammalian cells fixed between gold layers[63]. These breakthroughs have expanded the scope and capabilities of cryo-microscopy, facilitating the investigation and understanding of diverse biological and mineral specimens at fundamental scales.

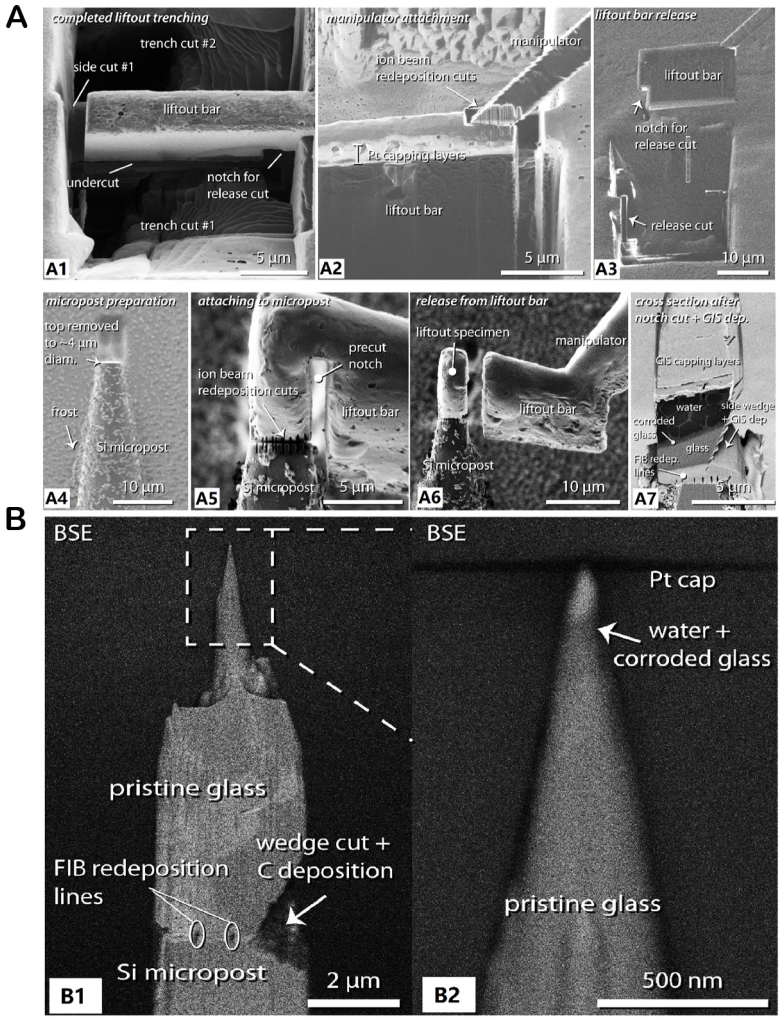

Figure 4. Micrographs from the cryogenic FIB lift-out process of a buried frozen water/solid interface: (A1) ROI trenching, (A2 and A3) lift-out, (A4) placing the lift-out bar on a silicon (Si) micropost, (A5) nano-welds by the re-deposition of the milled debris, (A6) detachment of the lift-out bar, and (A7) high-resolution image the cryo-specimen before annular milling. (B1) APT tip containing the interface of frozen water and corroded glass after annular milling, and (B2) the high-resolution image of (B1). Reproduced with the permission of Ref.[39] Copyright 2023, Elsevier.

RESEARCH ENABLED BY CRYO-APT

The advancements in cryo-transfer and cryo-specimen fabrication have resulted in groundbreaking scientific discoveries across various research fields. This section aims to showcase the successes achieved through the application of cryo-techniques, which have extended the utility of APT beyond its conventional areas of use.

Hydrogen in metals and alloys

Hydrogen can cause a reduction in the strength and ductility of metals and alloys, a phenomenon known as hydrogen embrittlement[64,65]. Understanding the location of hydrogen atoms in materials is crucial as it allows for correlations with microstructural sites that may be susceptible to hydrogen-induced cracks or capable of trapping detrimental hydrogen solutes, preventing them from participating in the embrittling process. This knowledge has given rise to a material design concept for hydrogen-embrittlement-resistant alloys, where hydrogen "traps" are introduced to create safe sites that can accommodate hydrogen solutes in

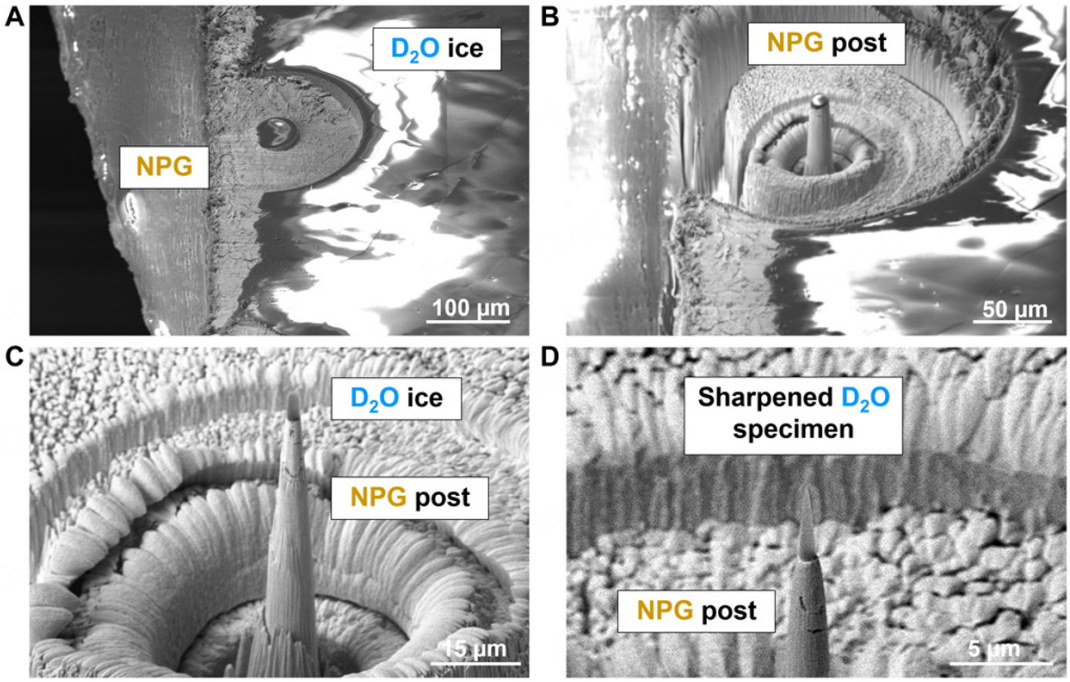

Figure 5. APT specimen preparation from a bulk nanoporous gold (NPG) with frozen heavy water (D_2O ice) in a plasma FIB. (A) NPG and D_2O ice before annular milling with the 200- and 75-µm milling patterns. (B) D_2O ice/NPG pillar during ion milling. (C) Ice/NPG tip after milling. (D) High-resolution view of the final APT tip. Reproduced with the permission of Ref.[32] Copyright 2023, Science Advances.

the metallic microstructure[66]. Among these traps, dispersoids, such as second-phase precipitates, are of great interest as they enhance material toughness while reducing the diffusible hydrogen content in the matrix[67].

APT exhibits exceptional sensitivity to light elements, including hydrogen, making it a promising technique for hydrogen mapping in materials. However, the high diffusivity of hydrogen in metals and alloys, regardless of the presence of traps, poses challenges, as hydrogen-charged metallic specimens are prone to desorption and signal loss. Recent advancements in cryo-transfer have enabled the study of frozen-in-place hydrogen atoms in metals and alloys using APT[40,46,68-73]. To ensure high-quality APT hydrogen analyses, a key experimental requirement is introducing deuterium (^{2}H or D) into APT tip specimens. Deuterium is a less-abundant isotope of hydrogen with a similar chemical reactivity but an additional neutron, resulting in higher atomic mass (and slightly lower diffusivity) than protium (^{1}H), the most abundant hydrogen isotope. Charging deuterium into APT specimens allows the distinction of experimentally introduced signals from the hydrogen background noise arising from the residual gas in the APT chamber[15]. While some studies have shown that using hydrogen charging can also provide qualitative measurements of hydrogen trapping[74], deuterium charging has been demonstrated to reduce ambiguity in observations[15]. Furthermore, deuterium charging must be combined with voltage-pulsed APT, as laser-pulsed APT can produce a significant amount of $^1H_2^+$ peak at 2 m/z, leading to confusion when assigning 2 m/z to deuterium ($^2H^+$)[75]. A comprehensive discussion on using APT for high-quality hydrogen mapping can be found in a recent review[15]. The following section will present several example findings made possible by cryo-APT.

Steels

In 2010, Takahashi *et al.* made a significant breakthrough by reporting the first high-resolution hydrogen mapping using APT in ferrite steel containing titanium carbides (TiC), as displayed in Figure 6A[73]. They achieved this successful analysis by employing a custom gaseous deuteration cell with thermal control on the APT tip specimens. This allowed for controlled heating during tip deuteration and subsequent quenching, facilitating the uptake of deuterium and minimizing its desorption thereafter. The study revealed that the trapped deuterium atoms (represented by red spheres in Figure 6A) were localized in regions where titanium and carbon atoms clustered, indicating hydrogen trapping at TiC. Subsequently, Takahashi *et al*. demonstrated another successful analysis of trapped deuterium atoms in vanadium carbides (VC) within a VC precipitation-strengthened steel, as shown in Figure 6B[76]. More recently, Takahashi *et al.* utilized cryo-APT to correlate VC-trapped deuterium with the crystal orientation of VC in a peak-aged VC steel, as depicted in Figure 6C[77]. This study provided valuable insights into the specific (001) plane trapping of deuterium in the VC, further expanding the capabilities of cryo-APT in unraveling intricate hydrogen-microstructure relationships. These studies showcase the potential of cryo-APT in advancing our understanding of hydrogen behavior in steels.

Apart from the work by Chen *et al.* have also made contributions to observing hydrogen trapping in steels[40]. Instead of using a custom gaseous charging deuteration cell, they opted for a route using heavy water electrolysis for tip deuteration[40]. This approach generated a substantially higher deuterium pressure (or fugacity) compared to the gaseous method used by Takahashi *et al.*, leading to improved data statistics of deuterium atoms in APT reconstruction[73]. This allowed for a more unambiguous observation of hydrogen trapping sites. As shown in Figure 7A, Chen *et al.* utilized cryo-APT to demonstrate the presence of trapped deuterium within vanadium-molybdenum-mixed (V-Mo) carbides, which possess a rocksalt (NaCl) structure in a ferritic steel matrix[40]. The left figure in Figure 7A represents a 10-nm-thick slice displaying deuterium and vanadium in red and blue, respectively. The right figure presents a statistical analysis, superimposing all identified V-Mo carbides from the APT dataset. This analysis reveals the distributions of deuterium in relation to other carbide-related elements (V, Mo, and C). The elemental distribution profile indicates that deuterium atoms mainly localize within the V-Mo carbides rather than at the interfaces of the carbides. As discussed, Chen *et al*. attributed this result to the presence of carbon vacancies in the V-Mo carbides[15].

Subsequently, Chen *et al*. applied the same experimental method to examine hydrogen trapping in niobium carbide (NbC) precipitates, as shown in Figure 7B[34]. Similar to the V-Mo carbides, the NbC also possesses a NaCl structure in a ferritic steel matrix but with fewer carbon vacancies. The top right figures in Figure 8B display 2-D slice views of the NbC precipitates and trapped deuterium (as schematized in the bottom left figure), revealing the hydrogen trapping at the NbC-ferrite interface. The bottom right figures in Figure 7B illustrate concentration profiles from two NbC precipitates (as schematized in the bottom left figure), confirming the interface hydrogen trapping of NbC. The combination of results from Figure 7A and B provides a comprehensive depiction of hydrogen trapping mechanisms in metal carbides with a NaCl structure. In addition, Chen *et al.* utilized cryo-APT to achieve the first-ever high-resolution observations of hydrogen segregation at dislocations and GBs, further demonstrating the power of cryo-APT in advancing research on hydrogen trapping and embrittlement in steels[34]. These groundbreaking findings have opened up new avenues for understanding the behavior of hydrogen in complex materials and its implications for material performance and design.

Aluminum alloys

Pristine aluminum (Al) and its alloys have a natural ability to form a protective aluminum oxide layer when exposed to oxygen, which shields them from further oxidation or corrosion. However, when these metals

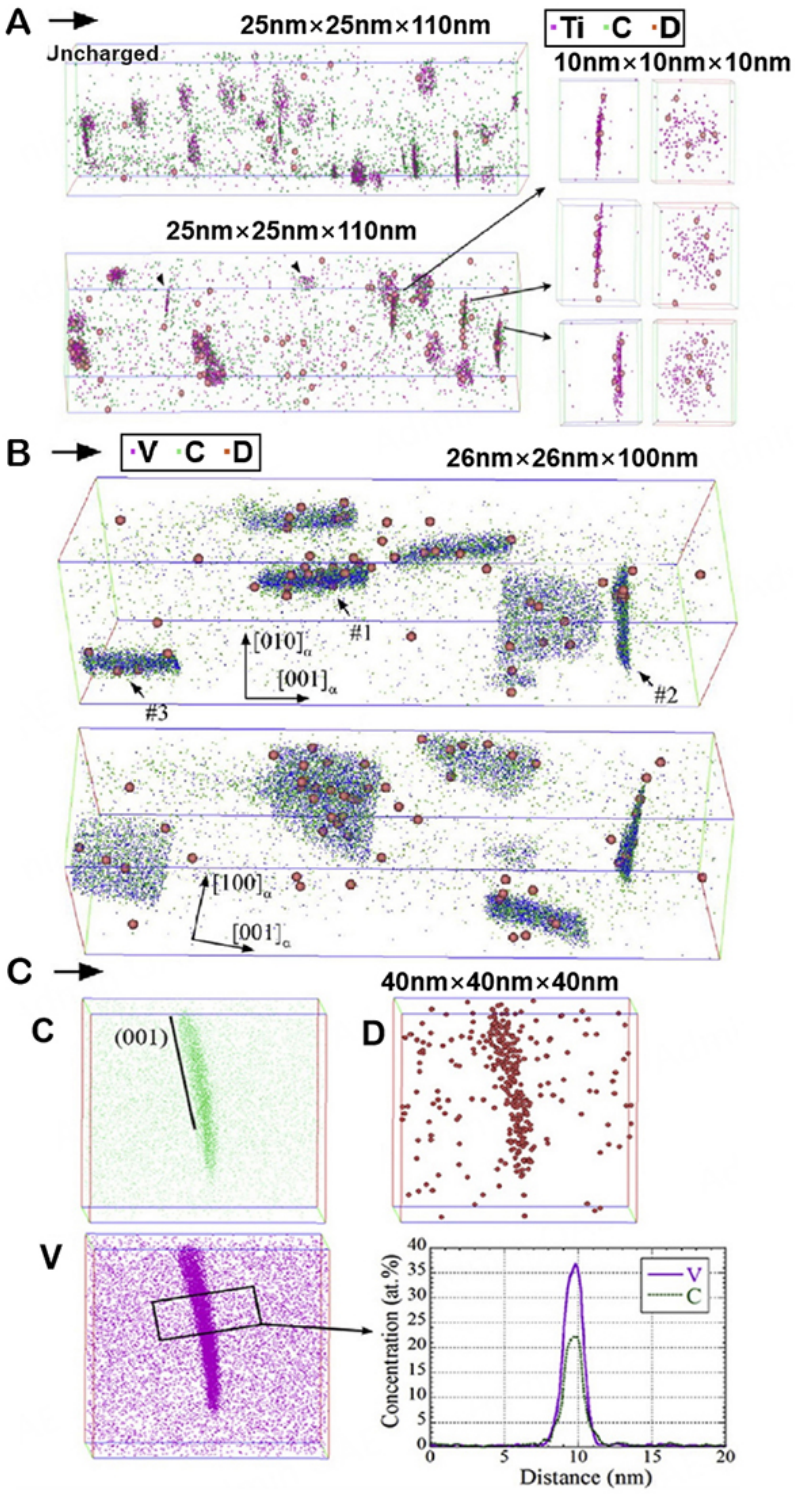

Figure 6. Observations of hydrogen (actually deuterium) atoms in steels by using cryo-APT. (A) 3-D atom maps of uncharged and deuterium-charged specimens of a TiC precipitation-strengthening steel. Reproduced with the permission of Ref.[73] Copyright 2010, Elsevier. (B) 3-D atom maps of deuterium-charged specimens of the VC precipitation steel. Reproduced with the permission of Ref.[76] Copyright 2012, Elsevier. (C) 3-D atom maps of a VC with trapped deuterium atoms. Reproduced with the permission of Ref.[77] Copyright 2018, Elsevier.

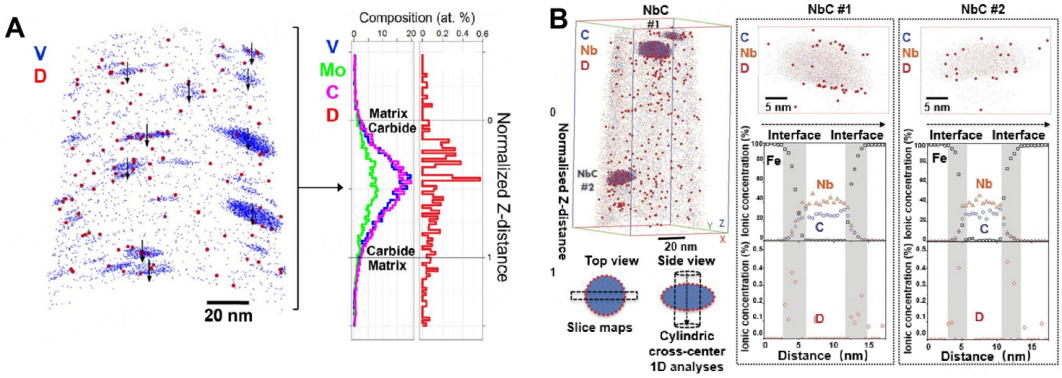

Figure 7. Cryo-APT observations of hydrogen trapping in metal carbides in ferrite steels. (A) APT analyses of a deuterium-charged ferritic steel containing V-Mo carbides. Reproduced with the permission of Ref.[40] Copyright 2017, The American Association for the Advancement of Science. (B) APT analyses of a deuterium-charged ferritic steel containing NbC. Reproduced with the permission of Ref.[34] Copyright 2020, The American Association for the Advancement of Science.

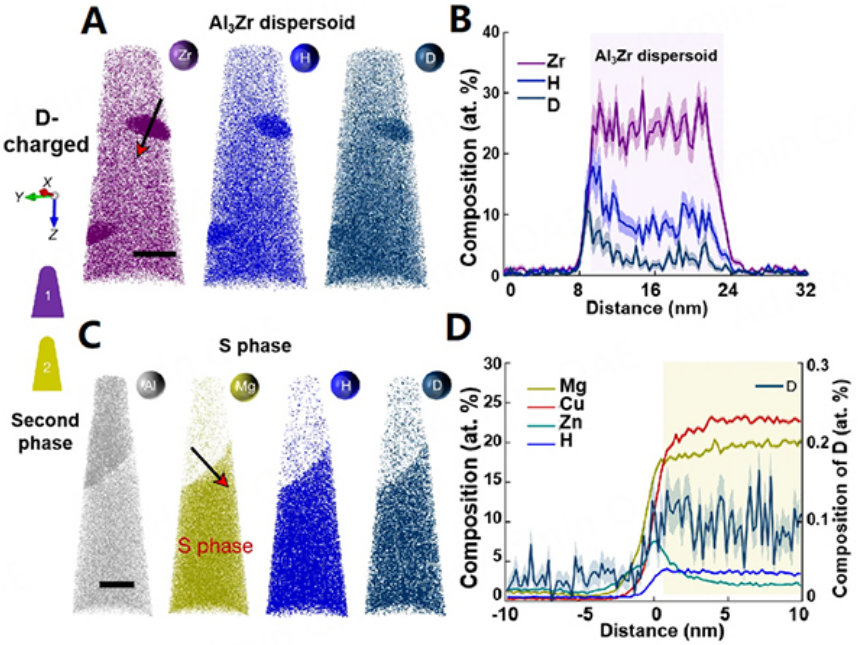

Figure 8. APT analyses deuterium-charged Al-Zn-Mg-Cu alloys. (A) 2-D slice views that include Al_3Zr dispersoids and (B) 1-D concentration profile from the arrow in (A). (C) 2-D slice views that include Al_2CuMg S phase and (D) 1-D concentration profile from the arrow in (C). Scale bars in (A, C) represent 30 nm. Reproduced with the permission of Ref.[79] Copyright 2022, Springer Nature.

come into contact with water (H_2O) or oxidize in a moist environment, hydrogen can be produced as a by-product during the oxidation process. This hydrogen can then permeate the metal matrix and lead to hydrogen embrittlement, compromising the mechanical properties of materials[78]. To enhance the microstructures of aluminum alloys and improve their resistance to hydrogen attack, it is crucial to investigate how hydrogen can be trapped within the material. Using APT plays a vital role in this endeavor.

Recently, Zhao *et al.* achieved success in using cryo-FIB to fabricate cryo-APT specimens and measure trapped deuterium in aluminum alloys[79]. The team provided the first direct observations of hydrogen trapping in Al_3Zr dispersoids (shown in Figure 8A and B) and the Al_2CuMg second phase (commonly

referred to as the S phase, shown in Figure 8C and D). Figure 8A reveals co-located clusters of Zr, a component of the Al_3Zr dispersoids, along with hydrogen (H) and deuterium (D), indicating that hydrogen and deuterium are trapped within these dispersoids. Figure 8B displays a 1-D concentration profile across the dispersoid, confirming the presence of trapped hydrogen and deuterium. Figure 8C presents atom maps showing the distribution of Al (matrix), Mg (S phase), and the trapped hydrogen and deuterium. Figure 8D shows the corresponding 1-D concentration profile from the region marked in the Mg map of Figure 8C. These findings offer valuable insights into the specific microstructures in aluminum alloys that have the capability to trap hydrogen, thus contributing to the development of materials that are more resistant to hydrogen embrittlement.

Titanium alloys

Titanium (Ti) alloys are highly sought after for aerospace applications due to their exceptional strength-to-weight ratio and corrosion resistance. However, Ti alloys are susceptible to hydrogen embrittlement, a phenomenon where hydrogen combines with the metal to form brittle hydride, leading to crack initiation and propagation[65]. Characterizing the hydride and its impact in Ti alloys using conventional FIB and APT has been challenging, primarily because of the rapid formation of hydrides during specimen preparation, such as in FIB, where hydrogen is often present as a residual gas in the environment. This tendency to absorb environmental hydrogen and form artifact hydrides has caused significant confusion in material characterization when trying to identify the true origin of hydrides.

As such, Chang *et al.* developed specimen preparation methods using cryo-PFIB and cryo-APT to analyze commercially pure Ti (CP Ti) and a Ti-6Al-2Sn-4Zr-6Mo alloy (referred to as Ti6246) in their pristine states[46]. The researchers employed hydrogen-sensitive APT to examine tip specimens prepared by electropolishing, conventional Ga FIB, Xe PFIB operating at room temperature, and cryo-PFIB. Their findings revealed that only cryo-PFIB provided hydride-free APT tips, as depicted in Figure 9. Figure 9A and B displays the CP-Ti and Ti6246 samples prepared using conventional FIB, showing the presence of artifact hydrides or significant hydrogen uptake from the FIB environment. On the other hand, Figure 9C and D demonstrates that using cryo-PFIB produced hydride-free APT results for CP-Ti and Ti6246, allowing for the analysis of the beta phase, which is prone to hydrogen uptake, with low hydrogen content [Figure 9D]. These results suggest a promising path to enhance the quality of high-resolution hydrogen analysis in Ti-based alloys by utilizing cryo-APT and cryo-FIB.

Liquid and organic specimens

The research in analyzing mobile hydrogen atoms in metals has showcased the capabilities of cryo-APT and cryo-FIB workflows to achieve low temperatures. This breakthrough has paved the way for their application in the analyses and preparation of biological specimens, which predominantly consist of water and have poor conductivity. However, the existing knowledge of APT and its instrumentation is primarily geared towards conductive materials, especially metals. How organic and ice specimens can behave in APT evaporation experiments is still largely unknown, which could impede the data interpretation in the 3-D atom reconstruction.

As such, Schwarz *et al.* conducted APT analysis on ice using cryo-specimen fabrication and laser-pulsed APT, resulting in the collection of several tens of millions of atoms, as shown in the mass spectrum in Figure 10A[80]. The analysis identified several primary peaks related to ice evaporation, with the top five peaks in relative intensity being H_3O^+ at 19 m/z, $(H_2O)H_3O^+$ at 37 m/z, $(H_2O)_2H_3O^+$ at 55 m/z, $(H_2O)_3H_3O^{2+}$ at 36.5 m/z, and $(H_2O)_3H_3O^+$ at 73 m/z (note the logarithmic scale). Building upon this achievement, Schwarz *et al.* performed another analysis on an aqueous solution saturated with glucose (chemical formula: $C_6H_{12}O_6$) to demonstrate the ability of APT to distinguish glucose peaks from ice peaks[81]. Figure 10B serves

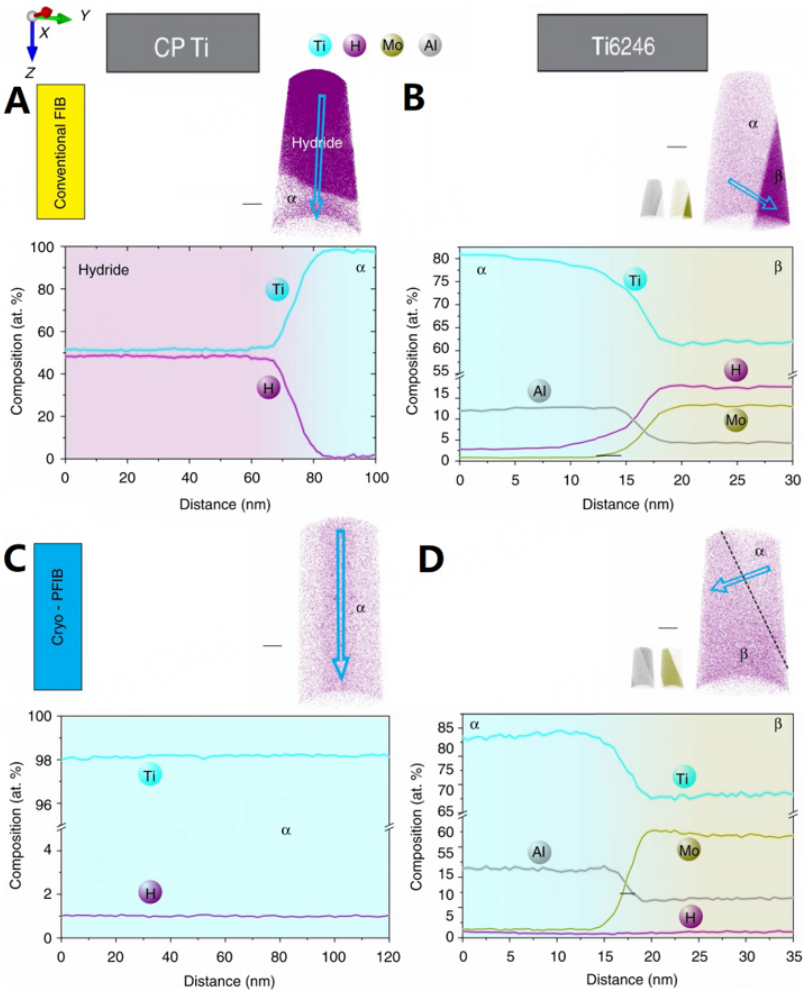

Figure 9. APT analyses of commercially pure Ti (CP Ti) and Ti6246 alloy. (A and B) are the atom maps and the corresponding concentration profiles of CP Ti and Ti6246, respectively, using conventional FIB specimen preparation at room temperature. (C and D) are the counterparts using cryo-PFIB, which show the low extent of hydrogen uptake from the specimen preparation processes. Scale bars are 20 nm. Reproduced with the permission of Ref.[46] Copyright 2019, Springer Nature.

as a reference for the peaks related to ice, displayed on a logarithmic scale. Figure 10C presents the peaks associated with glucose, with higher m/z (> 100 m/z), depicted on a linear scale, and these peaks are clearly distinguishable from the ice peaks. These results exemplify the potential of APT in studying organic species encapsulated in an ice APT tip. Following the successes, Meng *et al.* further utilized cryo-APT and cryo-FIB to analyze organic specimens, focusing on the fragmentation behavior of linear alkane chains, such as n-tetradecanes[42]. In their preliminary study, they discovered an extremely intricate fragmentation behavior, with numerous peaks associated with the C_xH_y ion species, where x can vary from 1 to 15. These findings open up new possibilities for studying organic compounds using cryo-APT and cryo-FIB techniques.

Schreiber *et al.* successfully employed the cryo-lift-out method (as shown in Figure 4) for cryo-APT specimens containing ice and non-homogeneous microstructures[39]. Their success resulted in the first APT dataset that captured an interface between alkaline solution corroded glass and ice from the solution. In Figure 11A, the 3-D reconstruction of the APT dataset is depicted with purple isoconcentration surfaces (isosurfaces), highlighting areas rich in lithium (Li) and sodium (Na) that reveal the chemical heterogeneity in the alkaline ice. Additionally, green calcium ions are displayed in Figure 11A, representing the location of

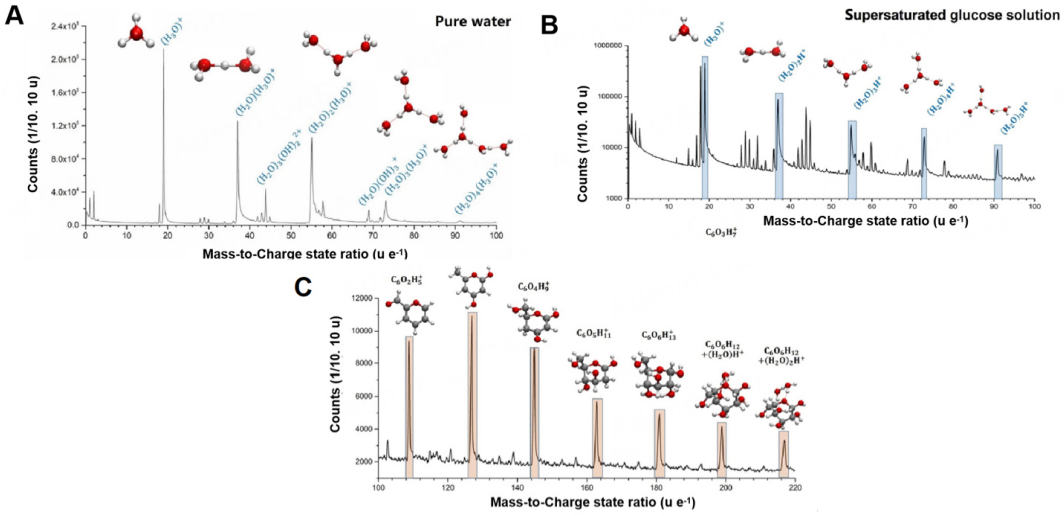

Figure 10. (A) APT mass spectrum of pure water. Reproduced with the permission of Ref.[80] Copyright 2020, Springer Nature. (B and C) are APT mass spectra of a supersaturated glucose aqueous solution in a logarithmic scale from 0 to 100 m/z and in a linear scale from 100 to 220 m/z, respectively. Reproduced with the permission of Ref.[81] Copyright 2021, Springer Nature.

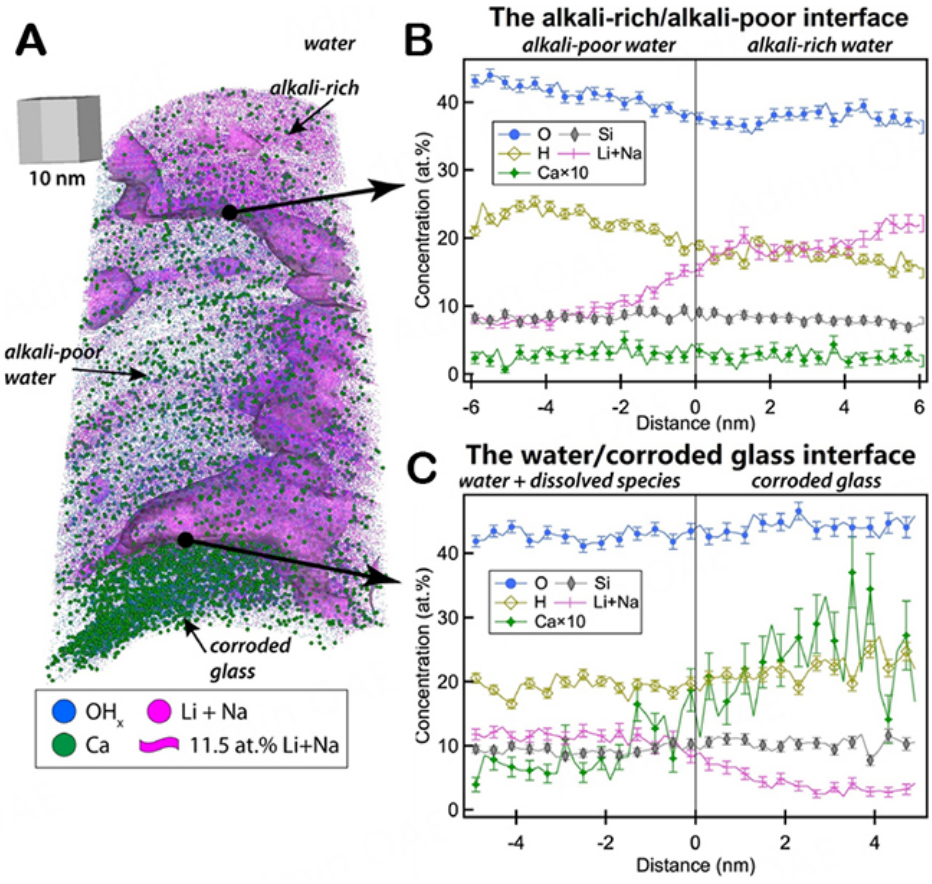

Figure 11. 3-D APT atom map and proximity histograms across the alkali-rich/alkali-poor interface in water and across the water/corroded glass interface. (A) 3-D APT atom map and proximity histograms across (B) the alkali-rich/alkali-poor interface in water and (C) across the water/corroded glass interface. Error bars indicate 1-sigma from standard counting error. Reproduced with the permission of Ref.[39] Copyright 2018, Elsevier.

the corroded glass substrate at the bottom and their presence in the top ice region from the alkaline solution. Figure 11B presents the proximity histogram (proxigram) of local composition, confirming the variance of Li + Na concentration (magenta) and distinguishing it from the concentration profiles of other non-background elements such as Si and oxygen (O). In Figure 11C, the proxigram of the local composition near the solution-glass interface confirms the high concentration of calcium (Ca), indicating the location of the glass substrate. These results demonstrate the power of combining cryo-APT and cryo-FIB to site-specifically capture microstructural features of interest in ice, thereby opening up new applications for these techniques in biological specimens, such as cells that primarily consist of water.

Energy storage materials

The push to develop long-lasting and high-capacity energy storage materials in order to reduce reliance on carbon-based fossil fuels has gained significant momentum. APT, with its ability to offer high-resolution mapping of light elements such as Li, holds great promise in this research field for developing improved battery materials[82].

However, when it comes to using APT for nanoscale Li mapping in battery materials, including anodes, cathodes, and electrolytes, a major challenge arises from in-situ delithiation and Li redistribution during APT experiments. The strong electrostatic field used in APT, along with the thermal migration caused by the laser beam, often leads to Li loss and inaccurate distribution in measurements, as observed in previous studies[83,84]. Since many battery materials are reactive to air or ambient moisture, using glovebox, vacuum transfer, and cryo-transfer for accurate measurement of Li distribution has been considered. However, Kim *et al.* found that neither vacuum nor cryo-transfer provided satisfactory APT measurements[85]. In one example dataset using a $LiNi_{0.8}Co_{0.1}Mn_{0.1}O_2$ (NMC811) cathode material and laser-pulsed APT with a specimen temperature of 60 K and low laser energy of 5 pJ, a nominally homogeneous distribution of Li was expected. However, a non-homogeneous distribution was measured, with higher Li concentration at the top and lower concentration underneath due to in-situ delithiation in APT [Figure 12A].

Interestingly, in Figure 12B, the authors observed contrasting results when the specimen was transferred in air and at room temperature, leading to the measurement of a nominally homogeneous Li distribution. They attributed this to the shielding effect of the surface layer, formed as a reaction with the ambient environment. Moreover, they found that cryo-FIB was necessary to prepare specimens with pristine compositions. In conclusion, Kim *et al.* emphasized the significance of electric-field shields and cryo-FIB, rather than cryo-APT, for obtaining high-quality APT results in Li mapping experiments[85]. These findings highlight the importance of carefully considering the specimen preparation methods and environmental factors in APT studies of battery materials.

Using the experimental cryo-FIB method developed by Singh *et al.* further used cryo-FIB for preparing APT tips from NMC811 particles, which is a Li-containing cathode material[86]. NMC811 particles are susceptible to corrosion in air, limiting their application in high-performance batteries. Additionally, similar to other lithium materials, NMC811 is also prone to electron beam damage during electron microscope observation, posing significant challenges in specimen preparation for APT.

To overcome these challenges, Singh *et al.* utilized the cryo-FIB method to prepare APT tips that incorporated the surface of an NMC811 particle [Figure 13A and B][86]. The particle was encapsulated in a chromium (Cr) layer deposited through physical vapor deposition (PVD) (shown in orange in Figure 13B). As a result, a layer consisting of Li, C, and O, representing corrosion products, was successfully captured in the APT data, as shown in Figure 13C. To provide detailed information about the composition of the layer,

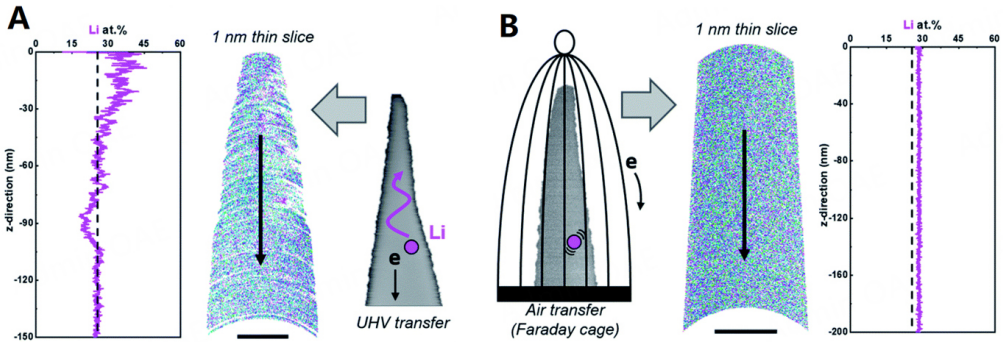

Figure 12. Li distribution of NMC811 specimens in APT. (A) APT data from a UHV transferred specimen with in-situ delithiation during the APT experiment. (B) APT data from an air-transferred specimen with the nominal Li composition and without delithiation, possibly due to the shielding effect of the surface corrosion product. The measurements were performed at a specimen temperature of 60 K and a pulsed laser energy of 5 pJ. Scale bars in (A and B) are 20 and 50 nm, respectively. Reproduced with the permission of Ref.[85] Copyright 2022, Royal Society of Chemistry.

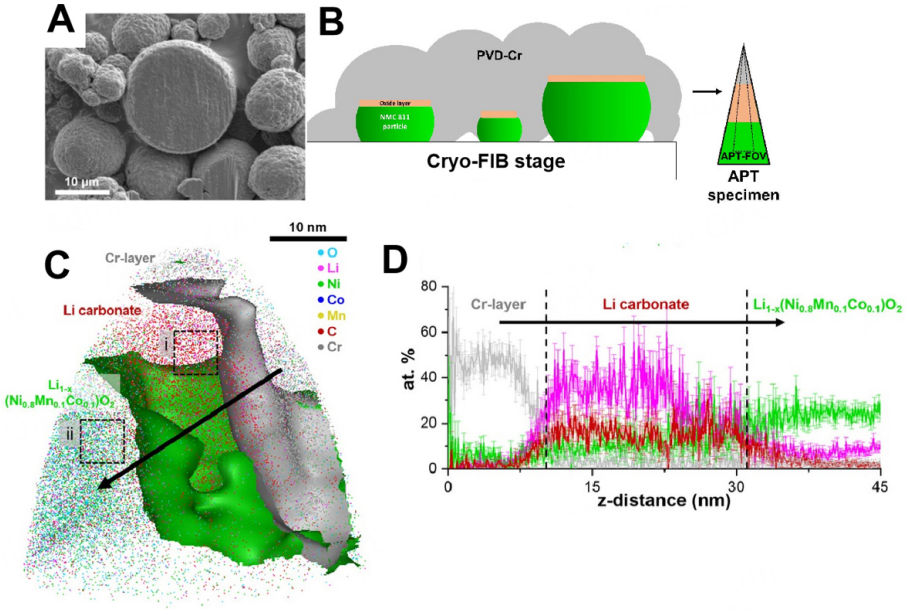

Figure 13. APT analysis of corroded $LiNi_{0.8}Mn_{0.1}Co_{0.1}O_2$ (NMC811) particle. (A) Scanning electron microscope image of the NMC811 particles. (B) Schematic illustrations of the APT specimen preparation method. The oxide layer of interest, as a corrosion product, is shown in orange. (C) 3-D reconstruction of the APT dataset of the tip incorporating the oxide later. (D) 1-D elemental concentration profile of the NMC oxide product from a cylindrical region of interest with 5 nm in diameter and 50 nm in length. Reproduced with the permission of Ref.[86] Copyright 2022, Wiley-VCH GmbH.

a 1-D concentration profile was generated from the region indicated in Figure 13C, as shown in Figure 13D. This direct evidence shed light on the chemical origin of the NMC811 corrosion, revealing that it is related to both oxygen and carbon, rather than solely oxygen. Such valuable insights were challenging to obtain using conventional electron microscopy techniques due to their limited ability to detect light elements. By employing cryo-FIB and APT in this study, Singh *et al.* demonstrated the power of these advanced techniques in providing crucial information on the corrosion behavior of NMC811 particles, which could contribute significantly to the development of more stable and efficient battery materials[86].

In battery research, there is a continuous effort to develop new anode materials that can outperform graphite, the current benchmark, while remaining cost-effective[87]. In 1976, Lai *et al.* suggested that Si could be a promising candidate for anodes, as it has the potential to store more lithium than graphite[88]. However, Si anode batteries suffer from poor charge-discharge cyclability due to significant volumetric changes during cycling, leading to cracking and degradation. There has been a lack of analytical techniques with sufficient spatial resolution to study the role of lithium in this degradation process, which hampers rational material design to address the issue.

Recently, Kim *et al.* made significant progress by utilizing cryo-FIB, cryo-transfer, and cryo-APT[89], based on the experimental method developed by El-Zoka *et al.* [Figure 5][32]. They applied the technique to analyze the elemental distribution in a battery system comprising a liquid electrolyte and a single-crystal Si anode after various charge-discharge cycles. In Figure 14A, the researchers successfully analyzed the frozen pristine liquid electrolyte, which contains 1 M $LiPF_6$ with a mixture of ethylene carbonate, $(CH_2O)_2CO$, and diethyl carbonate, $OC(OCH_2CH_3)_2$, in a 1:1 volume ratio, using cryo-APT. They also provided a reference APT dataset of the single-crystal Si [Figure 14A]. After one cycle, a fragment consisting of Si and Si oxide species (SiO_x) was found in the frozen liquid electrode, indicating Si anode degradation [Figure 14B]. After 25 cycles, Figure 14C revealed a GB of Si nanocrystalline decorated with SiO_x, confirmed by transmission electron microscope (TEM) analysis. These high-resolution elemental analyses of battery materials were made possible through the use of cryo-APT, which is sensitive to light elements, in combination with cryo-FIB, allowing the analysis of liquid samples. This breakthrough paves the way for more applications in advancing other lithium-based energy storage devices using liquid electrolytes.

LIMITATIONS AND OUTLOOK

This article emphasizes the potential of cryo-APT and its combination with cryo-FIB specimen preparation for providing nanoscale elemental mapping of materials. Several examples were presented to showcase its applications in researching hydrogen in metals, liquid and organic specimens, and Li battery materials. However, it is important to acknowledge the limitations of APT. Firstly, the cryo-APT and cryo-FIB instrumentation is still under development and not yet optimal. Integrating temperature-tracking into commercial LEAP and FIB systems for a complete thermal history of specimens remains challenging. This affects the quantitative measurement of specimen temperature and precise control of ice sublimation for high-quality biological specimen preparation[90].

Secondly, the data yield of APT experiments is limited by a high tip fracture rate. The success rate for analyzing hydrogen-charged steel tips is currently lower than 10%, and it can be even lower for less structurally robust specimens with heterogeneous interfaces or organic matter. Additionally, APT is a destructive technique, making it impossible to reproduce measurements on the same specimen. This leads to a comprehensive APT analysis being highly challenging and time-consuming. Thirdly, similar to other high-resolution microscopy techniques such as TEM, APT has a limited field of view 50 × 50 × 300 nm^3. Meaningful APT observations require more sampling compared to other imaging methods, further complicated by the low data yield due to the high fracture rate.

Despite these challenges, the future of cryo-APT looks promising, with various potential applications that can provide new insights in crucial scientific areas. For instance, a correlative imaging workflow can be developed to combine APT with TEM, enabling a direct correlation of hydrogen location and its effects[91,92]. It will also be interesting to correlatively apply imaging techniques that have wider fields of view than that of APT, such as X-ray-related techniques. This is vital for understanding hydrogen embrittlement and hydrogen storage. In analytical biology, cryo-FIB and cryo-APT can be utilized to study ionic transportation

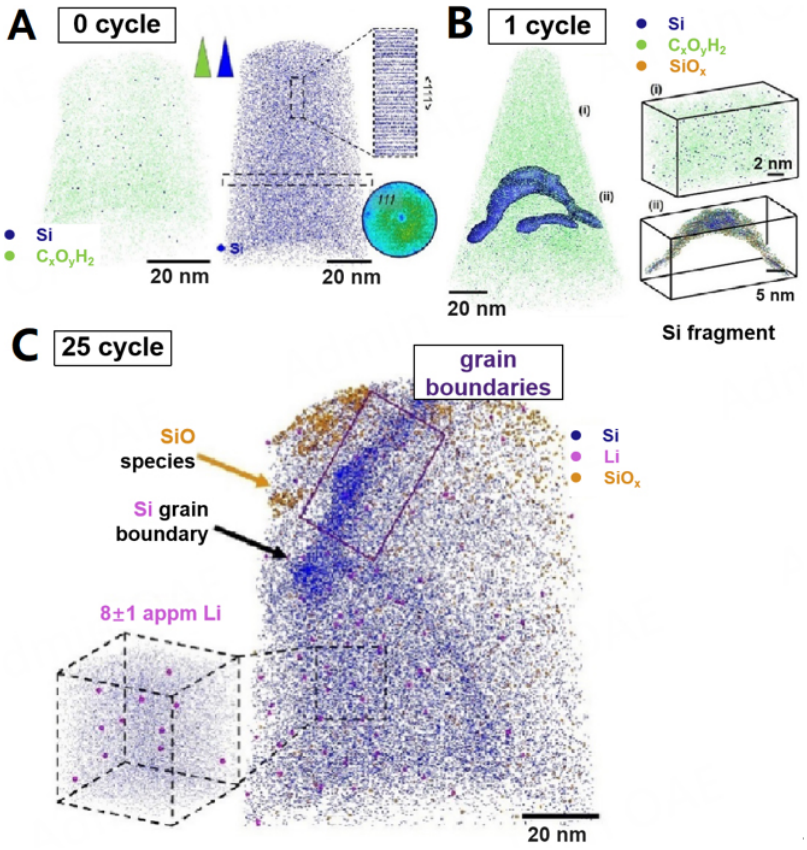

Figure 14. Cryo-APT (the protocol from Stephenson *et al.*[36], mentioned above), along with cryo-FIB (the protocol from[32], mentioned above), to understand the degradation of a model Si anode in a Li-ion battery at the atomic scale. (A) The result after 0 cycles; (B) The result after one cycle; (C) The result after 25 cycles. Reproduced with the permission of Ref.[89] Copyright 2022, ACS publications.

at the sub-cellular level, providing valuable information previously only accessible through nanoscale secondary ion mass spectrometry (NanoSIMS) with sub-micrometer resolution[93]. Moreover, the methods developed by Schreiber *et al.* and El-Zoka *et al.* offer a wide range of applications for studying corrosion in a liquid environment[32,39]. Additionally, as more laboratories adopt cryo-workflows for APT, the accessibility of cryo-APT is rapidly increasing, leading to its widespread recognition and impact across the scientific community in the near future.

DECLARATIONS

Authors' contributions

Drafted the manuscript: Zhou Z, Wang Z

Cairney participated the writing and literature discussion: Niu R, Liu PY, Huang C, Sun YH, Wang X, Yen HW, Cairney JM

Coordinated the writing and finalized the manuscript: Chen YS

Availability of data and materials

Not applicable.

Financial support and sponsorship

The authors gratefully acknowledge funding from the Australian Research Council (Grants IE230100160, LP210300999, LE190100048, LP180100431, and FT180100232), the CITIC-CBMM Nb Steel Award Fund

Program (2018FWNB30064), Taiwan's Ministry of Education (Taiwan-University of Sydney Scholarship), the National Science and Technology Council (111-2119-M-002-020-MBK), Microscopy Australia, and the University of Sydney's Core Research Facility program.

Conflicts of interest

All authors declared that there are no conflicts of interest.

Ethical approval and consent to participate

Not applicable.

Consent for publication

Not applicable.

Copyright

© The Author(s) 2023.

REFERENCES

1. Müller EW, Panitz JA, Mclane SB. The atom-probe field ion microscope. *Rev Sci Instrum* 1968;39:83-6. DOI
2. Gault B, Moody MP, Cairney JM, Ringer SP. Atom probe microscopy. Springer Science & Business Media; 2012. Available from: https://link.springer.com/book/10.1007/978-1-4614-3436-8 [Last accessed on 31 Oct 2023].
3. Miller MK, Forbes RG. The local electrode atom probe. Springer; 2014. Available from: https://link.springer.com/ chapter/10.1007/978-1-4899-7430-3_5 [Last accessed on 31 Oct 2023].
4. Lefebvre W, Vurpillot F, Sauvage X. Atom probe tomography: put theory into practice. Academic Press; 2016. Available from: https://shop.elsevier.com/books/atom-probe-tomography/lefebvre/978-0-12-804647-0 [Last accessed on 31 Oct 2023].
5. De Geuser F, Gault B. Metrology of small particles and solute clusters by atom probe tomography. *Acta Mater* 2020;188:406-15. DOI
6. Gault B, Chiaramonti A, Cojocaru-Mirédin O, et al. Atom probe tomography. *Nat Rev Methods Primers* 2021;1:51. DOI PubMed PMC
7. Kelly TF, Miller MK. Invited review article: atom probe tomography. *Rev Sci Instrum* 2007;78:031101. DOI PubMed
8. Geiser BP, Kelly TF, Larson DJ, Schneir J, Roberts JP. Spatial distribution maps for atom probe tomography. *Microsc Microanal* 2007;13:437-47. DOI PubMed
9. Müller EW. Resolution of the atomic structure of a metal surface by the field ion microscope. *J Appl Phys* 1956;27:474-6. DOI
10. Jacoby M. Atomic imaging turns 50. *Chem Eng News* 2005;83:13-6. Available from: https://cen.acs.org/articles/83/i48/Atomic-Imaging-Turns-50.html#:~:text=By%20the%20early%201950s%2C%20far,with%20a%20field%20ion%20microscope. [Last accessed on 31 Oct 2023]
11. Wagner A, Hall TM, Seidman DN. Simplified method for the calibration of an atom-probe field-ion microscope. *Rev Sci Instrum* 1975;46:1032-4. DOI
12. Brenner S, Mckinney J. Construction and performance of an FIM-atom probe. *Surf Sci* 1970;23:88-111. DOI
13. Kelly TF, Panitz JA. The first fifty years of atom probe. *Micros Today* 2017;25:12-7. DOI
14. Larson DJ, Prosa T, Ulfig RM, Geiser BP, Kelly TF. Local electrode atom probe tomography. New York: Springer Science; 2013. Available from: https://link.springer.com/content/pdf/10.1007/978-1-4614-8721-0.pdf [Last accessed on 31 Oct 2023].
15. Chen YS, Liu PY, Niu R, et al. Atom probe tomography for the observation of hydrogen in materials: a review. *Microsc Microanal* 2023;29:1-15. DOI
16. Grandfield K, Micheletti C, Deering J, Arcuri G, Tang T, Langelier B. Atom probe tomography for biomaterials and biomineralization. *Acta Biomater* 2022;148:44-60. DOI PubMed
17. Rajan K. Atom probe tomography - a high throughput screening tool for atomic scale chemistry. *Comb Chem High Throughput Screen* 2011;14:198-205. DOI PubMed
18. Miller M, Forbes R. Atom probe tomography. *Mater Charact* 2009;60:461-9. DOI
19. Silaeva EP, Karahka M, Kreuzer H. Atom probe tomography and field evaporation of insulators and semiconductors: theoretical issues. *Curr Opin Solid State Mater Sci* 2013;17:211-6. DOI
20. Reddy SM, Saxey DW, Rickard WDA, et al. Atom probe tomography: development and application to the geosciences. *Geostandard Geoanalytic Res* 2020;44:5-50. DOI
21. Liu J. Advances and applications of atomic-resolution scanning transmission electron microscopy. *Microsc Microanal* 2021;27:943-95. DOI
22. Thompson K, Lawrence D, Larson DJ, Olson JD, Kelly TF, Gorman B. In situ site-specific specimen preparation for atom probe tomography. *Ultramicroscopy* 2007;107:131-9. DOI PubMed
23. Tegg L, Breen AJ, Huang S, Sato T, Ringer SP, Cairney JM. Characterising the performance of an ultrawide field-of-view 3D atom

probe. *Ultramicroscopy* 2023;253:113826. DOI PubMed
24. Shen PS. The 2017 nobel prize in chemistry: cryo-EM comes of age. *Anal Bioanal Chem* 2018;410:2053-7. DOI
25. Moore EB, Molinero V. Structural transformation in supercooled water controls the crystallization rate of ice. *Nature* 2011;479:506-8. DOI PubMed
26. Dubochet J, Adrian M, Chang JJ, et al. Cryo-electron microscopy of vitrified specimens. *Q Rev Biophys* 1988;21:129-228. DOI
27. Gerstl S, Wepf R. Methods in creating, transferring, & measuring cryogenic samples for APT. *Microsc Microanal* 2015;21:517-8. DOI
28. Perea DE, Gerstl SSA, Chin J, Hirschi B, Evans JE. An environmental transfer hub for multimodal atom probe tomography. *Adv Struct Chem Imaging* 2017;3:12. DOI PubMed PMC
29. McCarroll IE, Bagot PAJ, Devaraj A, Perea DE, Cairney JM. New frontiers in atom probe tomography: a review of research enabled by cryo and/or vacuum transfer systems. *Mater Today Adv* 2020;7:100090. DOI PubMed PMC
30. El-Zoka AA, Stephenson LT, Kim SH, Gault B, Raabe D. The fate of water in hydrogen-based iron oxide reduction. *Adv Sci* 2023;10:e2300626. DOI PubMed PMC
31. Stender P, Gault B, Schwarz TM, et al. Status and direction of atom probe analysis of frozen liquids. *Microsc Microanal* 2022;28:1150-67. DOI
32. El-Zoka AA, Kim SH, Deville S, Newman RC, Stephenson LT, Gault B. Enabling near-atomic-scale analysis of frozen water. *Sci Adv* 2020;6:eabd6324. DOI PubMed PMC
33. Chen Y, Bagot PA, Moody MP, Haley D. Observing hydrogen in steel using cryogenic atom probe tomography: a simplified approach. *Int J Hydrog Energy* 2019;44:32280-91. DOI
34. Chen YS, Lu H, Liang J, et al. Observation of hydrogen trapping at dislocations, grain boundaries, and precipitates. *Science* 2020;367:171-5. DOI
35. Moody MP, Vella A, Gerstl SS, Bagot PA. Advances in atom probe tomography instrumentation: implications for materials research. *MRS Bull* 2016;41:40-5. DOI
36. Stephenson LT, Szczepaniak A, Mouton I, et al. The laplace project: an integrated suite for preparing and transferring atom probe samples under cryogenic and UHV conditions. *PLoS One* 2018;13:e0209211. DOI PubMed PMC
37. Miller MK. Atom probe microanalysis, principles and applications to materials problems. *Mater Res Soc* 1989. Available from: https://inis.iaea.org/collection/NCLCollectionStore/_Public/19/064/19064040.pdf?r=1 [Last accessed on 31 Oct 2023].
38. Melmed AJ. The art and science and other aspects of making sharp tips. *J Vac Sci Technol B* 1991;9:601-8. DOI
39. Schreiber DK, Perea DE, Ryan JV, Evans JE, Vienna JD. A method for site-specific and cryogenic specimen fabrication of liquid/solid interfaces for atom probe tomography. *Ultramicroscopy* 2018;194:89-99. DOI PubMed
40. Chen YS, Haley D, Gerstl SS, et al. Direct observation of individual hydrogen atoms at trapping sites in a ferritic steel. *Science* 2017;355:1196-9. DOI
41. Zachman MJ, de Jonge N, Fischer R, Jungjohann KL, Perea DE. Cryogenic specimens for nanoscale characterization of solid-liquid interfaces. *MRS Bull* 2019;44:949-55. DOI
42. Meng K, Schwarz TM, Weikum EM, Stender P, Schmitz G. Frozen *n* -tetradecane investigated by cryo-atom probe tomography. *Microsc Microanal* 2022;28:1289-99. DOI
43. Ackerman AK, Vorontsov VA, Bantounas I, et al. Interface characteristics in an α + β titanium alloy. *Phys Rev Mater* 2020;4:013602. DOI
44. Zhang S, Gervinskas G, Qiu S, et al. Methods of preparing nanoscale vitreous ice needles for high-resolution cryogenic characterization. *Nano Lett* 2022;22:6501-8. DOI
45. Lilensten L, Gault B. New approach for FIB-preparation of atom probe specimens for aluminum alloys. *PLoS One* 2020;15:e0231179. DOI PubMed PMC
46. Chang Y, Lu W, Guénolé J, et al. Ti and its alloys as examples of cryogenic focused ion beam milling of environmentally-sensitive materials. *Nat Commun* 2019;10:942. DOI PubMed PMC
47. Halpin JE, Webster RWH, Gardner H, Moody MP, Bagot PAJ, MacLaren DA. An in-situ approach for preparing atom probe tomography specimens by xenon plasma-focussed ion beam. *Ultramicroscopy* 2019;202:121-7. DOI PubMed
48. Marko M, Hsieh C, Schalek R, Frank J, Mannella C. Focused-ion-beam thinning of frozen-hydrated biological specimens for cryo-electron microscopy. *Nat Methods* 2007;4:215-7. DOI PubMed
49. Rigort A, Bäuerlein FJ, Villa E, et al. Focused ion beam micromachining of eukaryotic cells for cryoelectron tomography. *Proc Natl Acad Sci USA* 2012;109:4449-54. DOI PubMed PMC
50. Mahamid J, Schampers R, Persoon H, Hyman AA, Baumeister W, Plitzko JM. A focused ion beam milling and lift-out approach for site-specific preparation of frozen-hydrated lamellas from multicellular organisms. *J Struct Biol* 2015;192:262-9. DOI PubMed
51. Parmenter CD, Fay MW, Hartfield C, Eltaher HM. Making the practically impossible "merely difficult"-cryogenic FIB lift-out for "damage free" soft matter imaging. *Microsc Res Tech* 2016;79:298-303. DOI PubMed
52. Saxey DW, Cairney JM, McGrouther D, Honma T, Ringer SP. Atom probe specimen fabrication methods using a dual FIB/SEM. *Ultramicroscopy* 2007;107:756-60. DOI PubMed
53. Gordon LM, Joester D. Nanoscale chemical tomography of buried organic-inorganic interfaces in the chiton tooth. *Nature* 2011;469:194-7. DOI PubMed
54. Gordon LM, Tran L, Joester D. Atom probe tomography of apatites and bone-type mineralized tissues. *ACS Nano* 2012;6:10667-75. DOI PubMed

55. Gordon LM, Cohen MJ, MacRenaris KW, Pasteris JD, Seda T, Joester D. Dental materials. Amorphous intergranular phases control the properties of rodent tooth enamel. *Science* 2015;347:746-50. DOI PubMed
56. Fontaine A, Zavgorodniy A, Liu H, Zheng R, Swain M, Cairney J. Atomic-scale compositional mapping reveals Mg-rich amorphous calcium phosphate in human dental enamel. *Sci Adv* 2016;2:e1601145. DOI PubMed PMC
57. Langelier B, Wang X, Grandfield K. Atomic scale chemical tomography of human bone. *Sci Rep* 2017;7:39958. DOI PubMed PMC
58. Sundell G, Dahlin C, Andersson M, Thuvander M. The bone-implant interface of dental implants in humans on the atomic scale. *Acta Biomater* 2017;48:445-50. DOI PubMed
59. Prosa TJ, Keeney SK, Kelly TF. Atom probe tomography analysis of poly(3-alkylthiophene)s. *J Microsc* 2010;237:155-67. DOI PubMed
60. Rusitzka KAK, Stephenson LT, Szczepaniak A, et al. A near atomic-scale view at the composition of amyloid-beta fibrils by atom probe tomography. *Sci Rep* 2018;8:17615. DOI PubMed PMC
61. Perea DE, Liu J, Bartrand J, et al. Atom probe tomographic mapping directly reveals the atomic distribution of phosphorus in resin embedded ferritin. *Sci Rep* 2016;6:22321. DOI PubMed PMC
62. Sundell G, Hulander M, Pihl A, Andersson M. Atom probe tomography for 3D structural and chemical analysis of individual proteins. *Small* 2019;15:e1900316. DOI PubMed
63. Narayan K, Prosa TJ, Fu J, Kelly TF, Subramaniam S. Chemical mapping of mammalian cells by atom probe tomography. *J Struct Biol* 2012;178:98-107. DOI PubMed PMC
64. Martin ML, Connolly MJ, DelRio FW, Slifka AJ. Hydrogen embrittlement in ferritic steels. *Appl Phys Rev* 2020;7;041301. DOI PubMed PMC
65. Robertson IM, Sofronis P, Nagao A, et al. Hydrogen embrittlement understood. *Metall Mater Trans B* 2015;46:1085-103. DOI
66. Pressouyre G. Trap theory of hydrogen embrittlement. *Acta Metall* 1980;28:895-911. DOI
67. Bhadeshia HKDH. Prevention of hydrogen embrittlement in steels. *ISIJ Int* 2016;56:24-36. DOI
68. Chang Y, Breen AJ, Tarzimoghadam Z, et al. Characterizing solute hydrogen and hydrides in pure and alloyed titanium at the atomic scale. *Acta Mater* 2018;150:273-80. DOI
69. Chang Y, Zhang S, Liebscher CH, et al. Could face-centered cubic titanium in cold-rolled commercially-pure titanium only be a Ti-hydride? *Scr Mater* 2020;178:39-43. DOI
70. Haley D, Merzlikin S, Choi P, Raabe D. Atom probe tomography observation of hydrogen in high-Mn steel and silver charged via an electrolytic route. *Int J Hydrog Energy* 2014;39:12221-9. DOI
71. Breen AJ, Stephenson LT, Sun B, et al. Solute hydrogen and deuterium observed at the near atomic scale in high-strength steel. *Acta Mater* 2020;188:108-20. DOI
72. Sundell G, Thuvander M, Andrén HO. Hydrogen analysis in APT: methods to control adsorption and dissociation of H_2. *Ultramicroscopy* 2013;132:285-9. DOI PubMed
73. Takahashi J, Kawakami K, Kobayashi Y, Tarui T. The first direct observation of hydrogen trapping sites in TiC precipitation-hardening steel through atom probe tomography. *Scr Mater* 2010;63:261-4. DOI
74. Zhu X, Li W, Zhao H, Wang L, Jin X. Hydrogen trapping sites and hydrogen-induced cracking in high strength quenching & partitioning (Q&P) treated steel. *Int J Hydrog Energy* 2014;39:13031-40. DOI
75. Meier MS, Jones ME, Felfer PJ, Moody MP, Haley D. Extending estimating hydrogen content in atom probe tomography experiments where H_2 molecule formation occurs. *Microsc Microanal* 2022;28:1231-44. DOI
76. Takahashi J, Kawakami K, Tarui T. Direct observation of hydrogen-trapping sites in vanadium carbide precipitation steel by atom probe tomography. *Scr Mater* 2012;67:213-6. DOI
77. Takahashi J, Kawakami K, Kobayashi Y. Origin of hydrogen trapping site in vanadium carbide precipitation strengthening steel. *Acta Mater* 2018;153:193-204. DOI
78. Gangloff RP, Somerday BP. Gaseous hydrogen embrittlement of materials in energy technologies: the problem, its characterisation and effects on particular alloy classes. Elsevier; 2012. Available from: https://shop.elsevier.com/books/gaseous-hydrogen-embrittlement-of-materials-in-energy-technologies/gangloff/978-1-84569-677-1 [Last accessed on 31 Oct 2023].
79. Zhao H, Chakraborty P, Ponge D, et al. Hydrogen trapping and embrittlement in high-strength Al alloys. *Nature* 2022;602:437-41. DOI PubMed PMC
80. Schwarz TM, Weikum EM, Meng K, et al. Field evaporation and atom probe tomography of pure water tips. *Sci Rep* 2020;10:20271. DOI PubMed PMC
81. Schwarz TM, Dietrich CA, Ott J, et al. 3D sub-nanometer analysis of glucose in an aqueous solution by cryo-atom probe tomography. *Sci Rep* 2021;11:11607. DOI PubMed PMC
82. Devaraj A, Gu M, Colby R, et al. Visualizing nanoscale 3D compositional fluctuation of lithium in advanced lithium-ion battery cathodes. *Nat Commun* 2015;6:8014. DOI PubMed PMC
83. Pfeiffer B, Maier J, Arlt J, Nowak C. In Situ atom probe deintercalation of lithium-manganese-oxide. *Microsc Microanal* 2017;23:314-20. DOI PubMed
84. Greiwe GH, Balogh Z, Schmitz G. Atom probe tomography of lithium-doped network glasses. *Ultramicroscopy* 2014;141:51-5. DOI PubMed
85. Kim SH, Antonov S, Zhou X, et al. Atom probe analysis of electrode materials for Li-ion batteries: challenges and ways forward. *J Mater Chem A Mater* 2022;10:4926-35. DOI PubMed PMC

86. Singh MP, Kim SH, Zhou X, et al. Near-atomic-scale evolution of the surface chemistry in Li[Ni,Mn,Co]O_2 cathode for Li-ion batteries stored in air. *Adv Energy Sustain Res* 2023;4:2200121. DOI
87. McDowell MT, Lee SW, Nix WD, Cui Y. 25th anniversary article: understanding the lithiation of silicon and other alloying anodes for lithium-ion batteries. *Adv Mater* 2013;25:4966-85. DOI PubMed
88. Lai SC. Solid lithium-silicon electrode. *J Electrochem Soc* 1976;123:1196. DOI
89. Kim SH, Dong K, Zhao H, et al. Understanding the degradation of a model Si anode in a Li-ion battery at the atomic scale. *J Phys Chem Lett* 2022;13:8416-21. DOI PubMed PMC
90. Usukura J, Narita A, Matsumoto T, et al. A cryo-TSEM with temperature cycling capability allows deep sublimation of ice to uncover fine structures in thick cells. *Sci Rep* 2021;11:21406. DOI PubMed PMC
91. Kuzmina M, Herbig M, Ponge D, Sandlöbes S, Raabe D. Linear complexions: confined chemical and structural states at dislocations. *Science* 2015;349:1080-3. DOI PubMed
92. Huang L, Chen D, Xie D, et al. Quantitative tests revealing hydrogen-enhanced dislocation motion in α-iron. *Nat Mater* 2023;22:710-6. DOI
93. Greenwood DJ, Dos Santos MS, Huang S, et al. Subcellular antibiotic visualization reveals a dynamic drug reservoir in infected macrophages. *Science* 2019;364:1279-82. DOI PubMed PMC